Materials Science & Engineering A 971 (2026) 150575

Contents lists available at ScienceDirect

Materials Science & Engineering A

journal homepage: www.elsevier.com/locate/msea

Achieving superior performance of wire-directed energy deposited 316L stainless steel through the synergic effect of in-process high-pressure rolling and post-heat treatment

Yao Lu [a], Jun Wang [a,*], Hanxing Zhang [a], Jialuo Ding [b], Stewart Williams [a]

[a] Welding and Additive Manufacturing Centre, Cranfield University, MK43 0AL, UK
[b] WAAM3D Limited, 7 Thornton Chase, Linford Wood, Milton Keynes, MK14 6FD, UK

ARTICLE INFO

Keywords:
Wire-directed energy deposition
316L austenitic stainless steel
In-process high-pressure rolling
Microstructure
Mechanical property

ABSTRACT

316L austenitic stainless steel manufactured by wire-direct energy deposition (w-DED) typically exhibits coarse columnar solidification microstructures and pronounced anisotropy, which significantly limits its structural performance and engineering applicability. In this work, a cold high-pressure inter-layer rolling (HPR) strategy combined with post-deposition solution heat treatment is proposed as an effective and industrially viable thermo-mechanical route for microstructure and property control. Cold HPR introduces a large plastic strain at a low and well-controlled inter-pass temperature. This suppresses dynamic recovery during deposition and allows substantial stored strain energy to accumulate. As a result, the as-deposited microstructure evolves from a solidification-dominated state to a deformation-controlled state. The rolled components show pronounced deformation of the γ-austenite and fragmentation of the δ-ferrite. This deformation is accompanied by an increased fraction of low-angle grain boundaries and a higher dislocation density, which leads to significant strengthening. Subsequent heat treatment activates extensive static recrystallisation in the rolled samples. Fine equiaxed γ-austenite grains with high fractions of high-angle and Σ3 boundaries are formed, together with a strongly weakened crystallographic texture. This rolling + heat treatment synergy enables a broad and continuous mechanical property window and delivers a superior strength-ductility balance. The achieved performance surpasses most reported additively manufactured and wrought counterparts. Overall, the proposed cold HPR + heat treatment route provides a practical and flexible pathway for tailoring the performance of large-scale w-DED 316L components.

1. Introduction

Additive manufacturing (AM) has emerged as a promising approach for fabricating large-scale metallic components with complex geometries, offering advantages in terms of material efficiency, design flexibility, and near-net-shape production [1]. Among various AM techniques, directed energy deposition (DED) processes are particularly suitable for producing structural metal parts, owing to their high deposition rates and capacity for multi-material integration. Within this category, wire-directed energy deposition (w-DED) has received increasing attention as an efficient and cost-effective process, particularly for large-scale applications in the aerospace, energy, and marine sectors. In this process, metallic wire serves as the feedstock and is continuously melted and fed into a localised melt pool generated by a concentrated energy source, such as a plasma arc or laser. [2–5]. Compared with powder-based DED processes, w-DED offers higher material utilisation, improved operational safety, reduced costs, and simpler feedstock handling [1,5]. The advantages of w-DED are largely attributed to the use of metallic wire, by which material loss and contamination risk are minimised and stable deposition is ensured. The absence of powder-related issues such as oxidation, particle spatter, and stringent storage further enhances process robustness, making w-DED a promising route for producing large-scale, high-performance components [2,6].

Austenitic stainless steel 316L is widely used in critical structures due to its corrosion resistance, good toughness, and weldability [7–9]. In w-DED, 316L deposits typically exhibit coarse columnar grains, strong crystallographic texture, and high residual stresses, which originate

* Corresponding author.
E-mail address: jun.wang.123@cranfield.ac.uk (J. Wang).

https://doi.org/10.1016/j.msea.2026.150575
Received 30 March 2026; Received in revised form 3 June 2026; Accepted 6 June 2026
Available online 7 June 2026
0921-5093/© 2026 The Authors. Published by Elsevier B.V. This is an open access article under the CC BY license (http://creativecommons.org/licenses/by/4.0/).

from the intrinsic thermal characteristics of the process [10–12]. The combination of steep thermal gradients and directional solidification promotes epitaxial grain growth along the build direction [13]. Repeated thermal cycling further coarsens the grains and strengthens the texture, while non-uniform cooling induces heterogeneous residual stress distributions [11]. Consequently, mechanical anisotropy and reduced structural integrity are often reported in w-DED 316L components [14]. Besides, microstructural examinations of w-DED 316L have consistently revealed that the deposits possess an epitaxially grown coarse-grained structure which can adversely affect mechanical performance. Detailed studies have shown that, in the as-deposited state, δ-ferrite is distributed in skeletal, lath-like, or dendritic morphologies within the austenitic matrix, and the formation of σ phase has occasionally been reported [14,15]. Correspondingly, the tensile response of w-DED 316L exhibits orientation dependence, confirming the existence of strong mechanical anisotropy in the as-built material [16]. Several of these issues can be mitigated by post-processing. Hot isostatic pressing is commonly applied to relieve residual stress, close porosity, and, in some cases, promote recrystallisation [17]. However, such a measure would cause additional cost and lead time, and its effectiveness is limited for large-scale components, where columnar grains and anisotropy may persist. Consequently, in-process microstructural control is considered more effective. Approaches implemented during deposition can disrupt epitaxial growth, refine grains, and regulate stress evolution, which are essential for ensuring the reliability of w-DED 316L components [18,19].

In this context, in-process mechanical deformation, particularly rolling during deposition, has been explored as an effective strategy to refine grains, promote dynamic recrystallisation (DRX) [20], and release residual stresses [18]. In 2023, Xu et al. integrated an in-situ hot-rolling unit into a wire arc additive manufacturing (WAAM) system and applied a compressive load of about 8 kN, with the inter-layer rolling temperature reported to be approximately 810-830 °C [18]. In 2022, Kan et al. mounted a layer-by-layer rolling head on a laser DED platform, where the substrate was lowered after each pass to maintain contact with the roller and rolling forces of 0.75-4 kN were applied immediately after deposition [21]. Lastly in 2024, Liu et al. developed a laser-directed energy deposition and ultrasonic rolling (LDED-UR) hybrid system in which an ultrasonic transducer, booster and roller were rigidly connected to the laser head to impose static pressure combined with high-frequency vibration during deposition [22]. Elmer et al. further showed that mechanical rolling followed by annealing substantially decreased texture intensity and mechanical anisotropy in w-DED 316L [23]. These findings highlight the potential of deformation-assisted additive manufacturing for enhancing performance. Nevertheless, previous studies have mainly implemented rolling under high-temperature and low-load conditions. Such hot rolling introduced only limited plastic strain under small forces (<10 kN) [21]. In these setups, the roller was typically positioned directly behind the deposition torch and therefore continuously exposed to the high thermal environment of the melt pool, which could cause severe thermal damage and shorten tool life. Moreover, the temperature distribution within the deposited layers was difficult to monitor and control, making it challenging to maintain consistent deformation conditions. In addition, the rolling strategies employed in these studies are largely limited to simple, planar geometries [23]. When applied to complex components, particularly at corners, intersections, or regions with abrupt geometric changes, the rolling tools struggle to deliver sufficient and homogeneous deformation. As a result, rolling effectiveness in these critical regions is often compromised. These limitations have constrained the practical scalability of in-process rolling and hindered systematic investigations of deformation effects.

In contrast, this work employs a cold inter-layer rolling strategy with a fixed inter-pass temperature of approximately 150 °C, applied after the deposition of each layer. This approach eliminates the need for continuous heating, thereby avoiding thermal damage to the roller and simplifying system control. A series of systematically varied rolling loads (40, 80, and 120 kN) was applied to establish a wide deformation range, enabling clear observation of the progressive microstructural evolution and corresponding mechanical response. Furthermore, by coupling the in-process rolling with subsequent heat treatment, the process allows for precise tuning of mechanical properties through controlled strain introduction and thermal recovery. This study provides optimised deformation-assisted additive manufacturing strategies for high-performance 316L stainless steel components, whilst also providing new insights into the process-structure-property relationships in large-scale metal additive manufacturing.

2. Experimental procedure

In this experiment, austenitic stainless steel 316L solid wire with a diameter of 1.2 mm was used as the feedstock. The nominal chemical composition (wt.%) is: Cr 16–18, Ni 10–14, Mo 2–3, Mn $\leq$ 2, Si $\leq$ 1, C $\leq$ 0.03, P $\leq$ 0.045, S $\leq$ 0.03, N $\leq$ 0.10, Fe balance. Deposition was carried out on a 316L stainless steel substrate using a plasma-based w-DED system, which was powered by an EWM plasma arc source and integrated on a KUKA six-axis robot for controlled motion (see Fig. 1). The total wall height was designed to be 40 mm. The key deposition parameters were maintained constant for all builds: current of 200 A, wire feed speed (WFS) of 2.35 m/min, and travel speed (TS) of 3.3 mm/s. The plasma shielding gas with a flow rate of 0.8 L/min was employed to ensure stable arc behaviour. The detailed process parameters are displayed in Table 1. Besides, Argon shielding gas along with a local shielding device (Fig. 1(b)), was employed to minimise oxidation during deposition.

The CNC rolling system with a hydraulically actuated roller was applied to introduce an inter-layer rolling process, as illustrated in Fig. 1 (b). A normal load was applied and monitored through an integrated hydraulic cylinder with force-sensing capability. Four rolling conditions were investigated, which are 0 kN (unrolled), 40 kN, 80 kN, and 120 kN. These conditions enabled the evaluation of the effect of varying rolling loads on microstructural evolution and mechanical performance. After deposition, specimens were sectioned for both microstructural evaluation and mechanical testing. For metallographic observation, cross-sectional samples were extracted from the mid-length of each wall. These samples were used to analyse the bead geometry and grain information. The macrostructural observation was carried out by the Hirox Digital Optical Microscope System. The microstructural analyses were performed using optical microscopy (OM, Zeiss Axiolab 5), scanning electron microscopy (SEM, TESCAN VEGA 4), and electron backscatter diffraction (EBSD, TESCAN S8000G). Electrolytic etching was carried out by an oxalic acid solution prepared by dissolving 10g of oxalic acid in 100 mL of distilled water under 6V DC using a stainless-steel cathode. For mechanical property testing, tensile coupons with a gauge length of 25 mm (according to ASTM E8/E8M standard) were machined parallel to the build direction from each wall. The extraction locations were kept consistent among all rolling conditions to ensure comparability. The surface of each tensile specimen was ground and polished prior to testing to minimise surface defects introduced during machining. Tensile testing was done at room temperature using a testing machine (Instron 4467 30 kN electromechanical frame) with a loading rate of 1 mm/min. In addition, hardness testing was realised by the Innovatest Falcon 503 machine with a load of 300g. Whereafter, a heat treatment (HT) process was conducted by heating the specimens to 1100 °C at a controlled heating rate of 20 °C/s, followed by a 1.5 h holding stage at the target temperature. After soaking, the samples were air-cooled to room temperature. This procedure was applied to assess whether the mechanical rolling-induced deformation could be further utilised through thermal activation to improve the microstructure and mechanical properties.

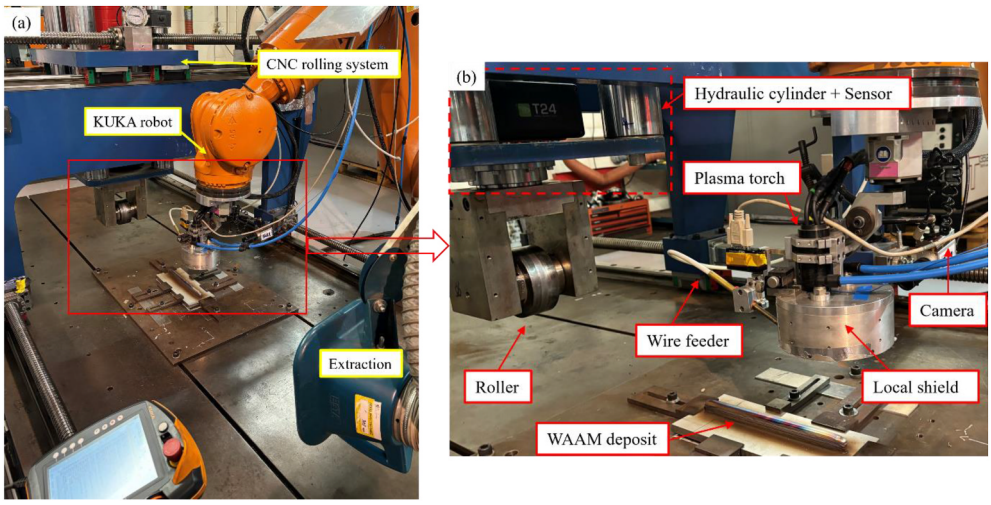

Fig. 1. Robotic plasma-based w-DED system with integrated in-process rolling: (a) overall workstation; (b) end-effector assembly including plasma torch, hydraulically actuated roller, wire feeder, and local shielding device.

Table 1
Key deposition parameters for all conditions.

Process parameters	Value
Wire feeding speed (WFS)	2.35 m/min
Torch travel speed (TS)	3.3 mm/s
Inter-layer temperature	150 °C
Current (A)	200 A
Nozzle to substrate stand-off	8 mm
Plasma gas flow rate	0.8 L/min
Local shielding flow rate	60 L/min
Wire feeding angle	25°
Rolling loads	0/40/80/120 kN

3. Results and discussion

3.1. Macrostructural characteristics

The top and front views of the walls fabricated under different rolling forces are shown in Fig. 2. The unrolled wall exhibits a relatively uniform surface (Fig. 2(a)). With increasing rolling force from 40 to 120 kN (Fig. 2(b–d)), the surface becomes progressively smoother, and the deposited layer contours become more regular and better consolidated. The front views show reduced waviness and flatter interfaces. A gradual inclination of the wall toward the rolling direction is also observed with increasing load, which can be attributed to asymmetric plastic deformation and the resulting bending moment within the thin-walled structure [24,25]. In terms of size, all walls maintain similar geometry, with a length of about 270 mm and a height of around 40 mm. Importantly, no visible microcracks were observed, confirming that the applied rolling forces did not cause structural damage.

Fig. 3 shows the cross-sectional macrostructures on the building direction (BD)–normal direction (ND) plane, which is perpendicular to the rolling direction (RD), and the dimensional changes of the walls deposited under different rolling forces, indicating a clear change in wall geometry with increasing rolling intensity. All samples were deposited to a nominal height of approximately 40 mm. In the unrolled condition, the wall maintains a relatively narrow width and wide thickness, typical of the layer-by-layer deposition process dominated by surface tension and molten pool shape. When interlayer rolling is applied, the newly deposited layer experiences solid-state plastic compression under the applied contact pressure. To accommodate the thickness reduction, material is displaced outward from the roller track, leading to a measurable increase in wall width and a decrease in layer thickness.

As the rolling force increases, the wall exhibits increasing widening together with a corresponding decrease in layer thickness (see Fig. 3(e)). Mechanically, this widening arises from a combination of compressive plastic deformation and constrained flow [26,27]. Consequently, the imposed rolling strain modifies the as-deposited structure through

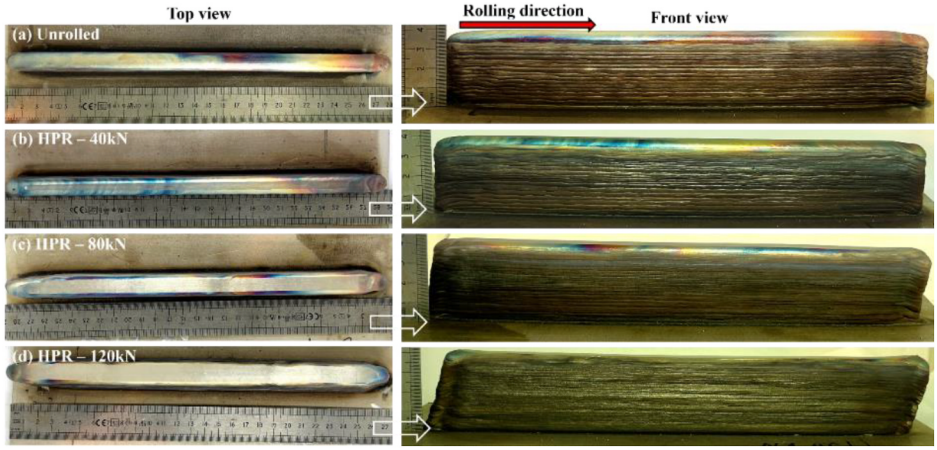

Fig. 2. Macro-morphologies of w-DED 316L walls deposited under different rolling forces: (a) Unrolled, (b) HPR-40 kN, (c) HPR-80 kN, and (d) HPR-120 kN. (HPR: High Pressure Rolling).

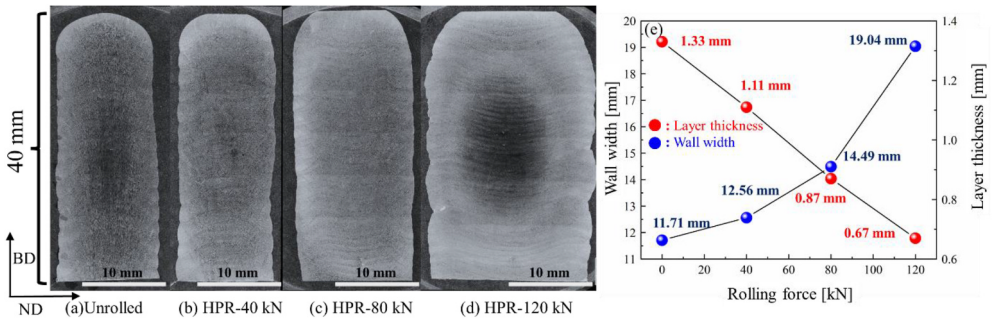

Fig. 3. Cross-sectional morphologies of the walls deposited under different rolling forces: (a) Unrolled, (b) HPR-40 kN, (c) HPR-80 kN, (d) HPR-120 kN, and (e) variation of wall width and layer thickness as a function of rolling force.

plastic deformation and stored energy accumulation, thereby facilitating subsequent microstructural refinement.

3.2. *Microstructural characteristics in the as-deposited condition*

Optical micrographs in Fig. 4 reveal that the microstructure of all samples is composed of γ-austenite in light contrast as the matrix and a small fraction of δ-ferrite in dark contrast distributed along solidification boundaries and grain boundaries, which is consistent with previous studies [14,28]. The examined regions were selected from the mid-height of the walls to minimise the effects of top or bottom layers. In the unrolled condition (Fig. 4(a and b)), elongated γ grains grow epitaxially across multiple layers, and the interlayer boundary exhibits a curved molten-pool profile characteristic of solidification-driven growth. With the introduction of in-process rolling (Fig. 4(c–h)), the initially curved interlayer regions are progressively straightened under compressive loading. In addition, the γ-austenite morphology deviates from its fully columnar form due to the plastic deformation caused by rolling [9]. The δ-ferrite dendritic arms become compressed, bent, and locally truncated, particularly near the interlayer zones. The δ-ferrite remains distributed along solidification boundaries but becomes elongated perpendicular to BD and partially fragmented under deformation. Nevertheless, the microstructure remains entirely solidification-derived at the optical scale. The progressive straightening of the interlayer boundaries corresponds directly to the reduction in layer waviness observed in Figs. 2 and 3. Simultaneously, the distortion and segmentation of the dendritic substructure provide a microstructural basis for subsequent strain accumulation, misorientation development, and potential recrystallisation, which will be examined through EBSD in the next section. In addition, the representative EBSD results shown in Fig. 4 (i and j) confirms that the microstructure consists predominantly of FCC austenite together with a small fraction of BCC phase distributed along the interdendritic regions, supporting the identification of the dark-contrast interdendritic phase as δ-ferrite.

The EBSD inverse pole figure (IPF) maps in Fig. 5 provide quantitative insight into the austenite grain-scale response of w-DED 316L under different HPR processes. The analysis was conducted on mid-height cross-sections in the BD–ND plane, perpendicular to the RD. In

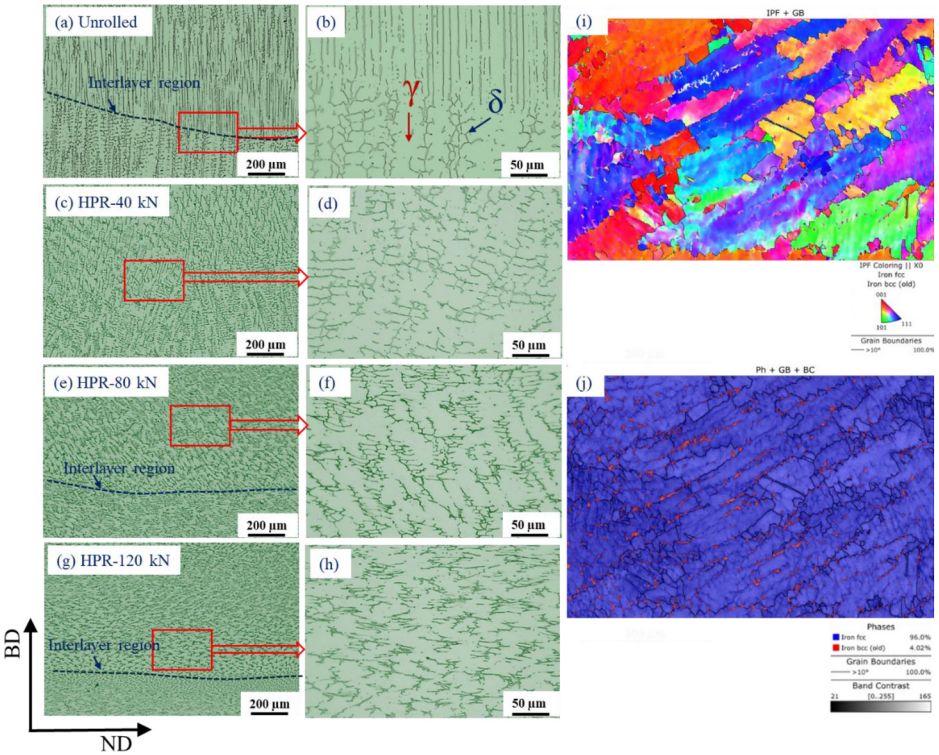

Fig. 4. Optical microstructures (OM) of w-DED 316L walls deposited under different rolling forces: (a-b) Unrolled, (c-d) HPR-40 kN, (e-f) HPR-80 kN, (g-h) HPR-120 kN, (i) representative EBSD inverse pole figure map, and (j) corresponding phase map showing an FCC austenitic matrix together with a small fraction of BCC phase (δ-ferrite) distributed along the interdendritic regions.

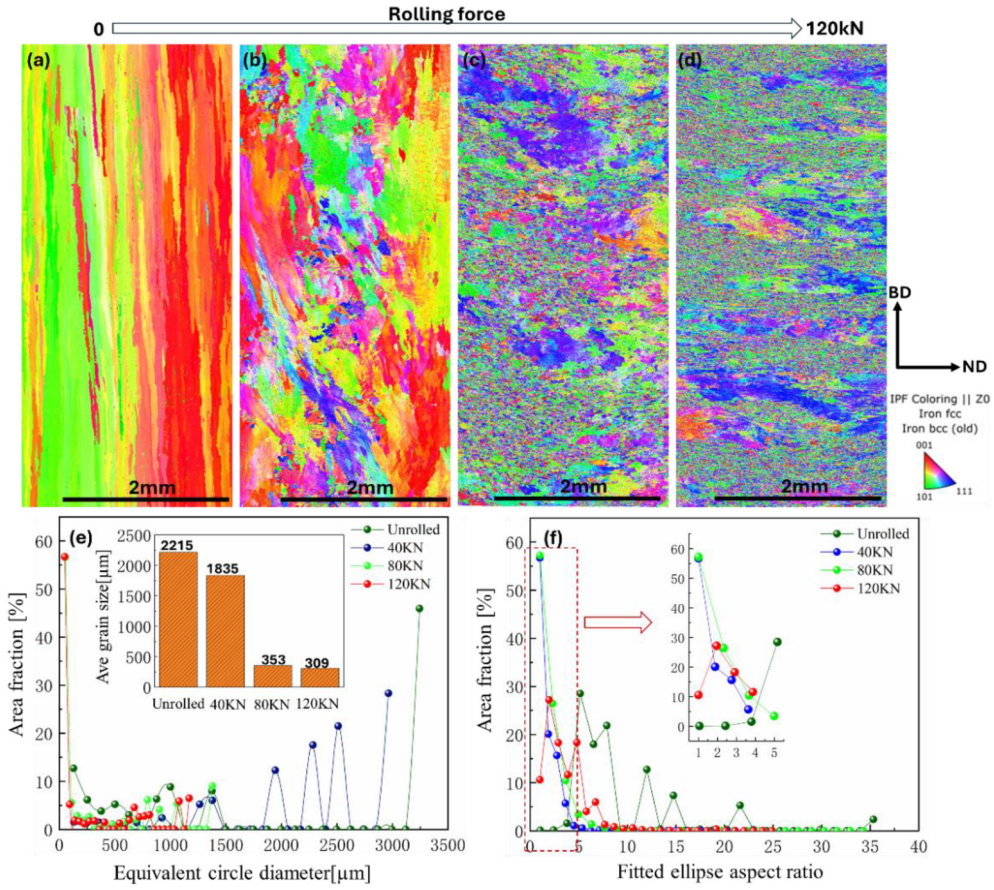

Fig. 5. Inverse pole figure (IPF) maps under various rolling conditions: (a) Unrolled, (b) HPR-40kN, (c) HPR-80kN, and (d) HPR-120kN; (e) comparison of equivalent circle diameter distributions in different conditions; (f) comparison of fitted ellipse aspect ratio distributions in different conditions.

the unrolled condition (Fig. 5(a)), the microstructure is dominated by millimetre-scale columnar γ-austenite grains growing epitaxially along the BD. This strongly oriented solidification structure is typical for w-DED deposition, where heat accumulation promotes epitaxial extension across multiple layers [29]. When a moderate rolling load of 40 kN is applied (Fig. 5(b)), the initially continuous columnar arrays become distorted and fragmented. The IPF colour contrast reveals increasing orientation variation, indicating the onset of sub-grain formation and the partial breakdown of epitaxial continuity. This phenomenon is consistent with the deformation-driven reorientation observed in other rolled or peened austenitic systems [18]. At 80 kN and 120 kN (Fig. 5(c and d)), the columnar γ grains are completely disrupted, forming a non-uniform grain structure consisting of alternating bands of finely equiaxed grains, small columnar and pancaked grains in between the bands. Such a duplex grain structure suggests that interlayer rolling introduced significant plastic deformation and stored energy, while the repeated reheating associated with subsequent layer deposition may have promoted local recovery and recrystallisation in the deformed regions. However, this microstructural evolution was not spatially complete throughout the deposited wall. The preferential alignment along the BD is largely lost, indicating that the high compressive strain effectively suppresses competitive grain growth and enhances geometrical fragmentation. Similar morphology transitions have also been reported for in-process deformation-assisted additive manufacturing [18, 22].

In addition, quantitative grain-size statistics (Fig. 5(e)) confirm an obvious refinement trend. The gradual contraction of the size distribution indicates that large, solidification-derived grains are progressively replaced by smaller, strain-modified segments. Further, grain-shape analysis (Fig. 5(f)) shows a consistent evolution. The fitted-ellipse aspect ratio (AR) result exhibits a high-AR tail (>15) in the unrolled condition, reflecting the elongated columnar geometry. With increasing rolling force, the distribution shifts toward low AR values (~1-3), which illustrates a significant columnar-to-equiaxed transition driven by interlayer rolling.

The kernel average misorientation (KAM) maps in Fig. 6 show how local strain evolves with increasing rolling load through the competition between deformation introduced by interlayer rolling and the partial recrystallisation triggered during subsequent deposition [30]. In the unrolled sample (Fig. 6(a)), most regions exhibit a generally dark blue colouring, corresponding to KAM values below 1°. The distribution curve (Fig. 6(e)) shows a sharp peak near zero misorientation, indicating limited lattice distortion and a solidification-dominated microstructure. However, pronounced high-strain bands shown in light blue still can be observed align along BD. These elevated KAM values arise because the δ-ferrite network accumulates solidification- and transformation-induced residual stresses, and its higher stiffness limits stress relaxation compared with the surrounding γ austenite [31]. At 40 kN, rolling introduces substantial deformation strain, but the deposition of the next layer partially remelts the surface and reheats the underlying material into a temperature window that activates partial recrystallisation. Consequently, although deformation-induced misorientation is introduced, reheating reduces and redistributes much of this strain. As such in-situ recrystallisation is incomplete, a moderate level of deformation strain is still retained. At 80 kN, stronger rolling produces a higher density of stored energy and dislocations. Subsequent reheating again promotes grain refinement and partial recrystallisation, which reduces the local strain within the recrystallised equiaxed regions. However, regions that do not fully recrystallise preserve significant deformation-induced misorientation. This contrast between low-strain

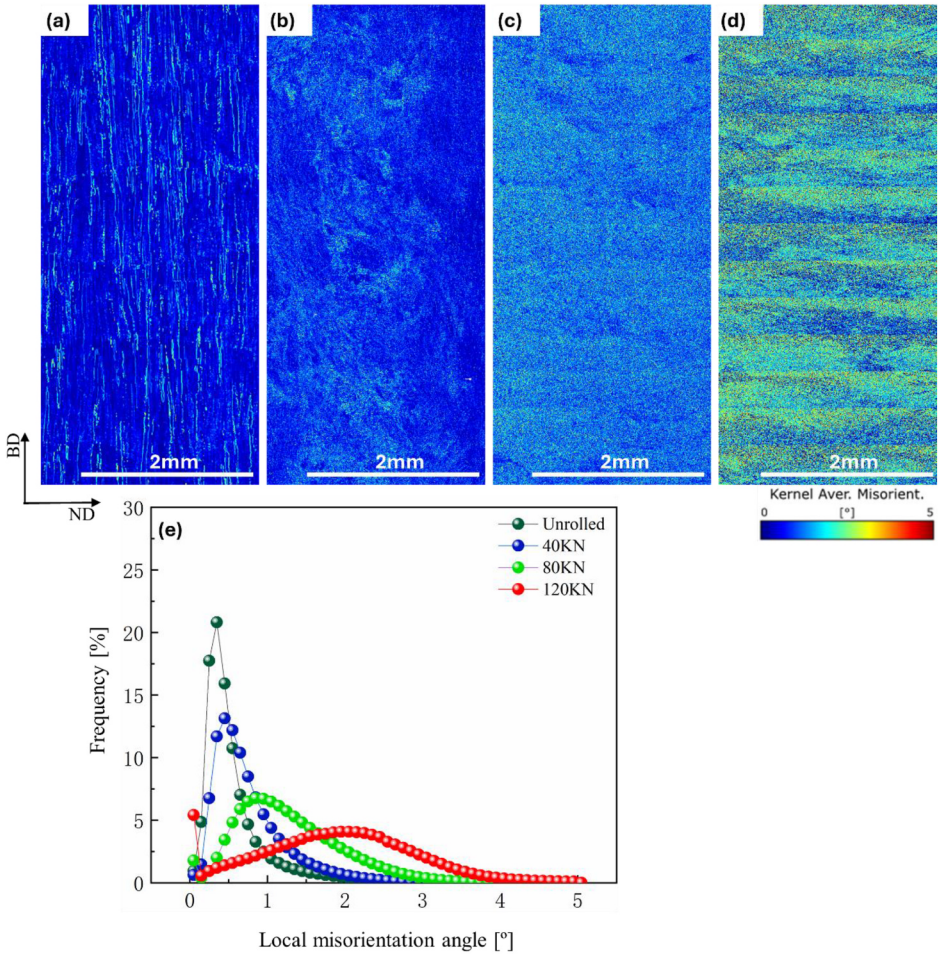

Fig. 6. Local misorientation maps at conditions of (a) Unrolled, (b) HPR-40kN, (c) HPR-80kN, (d) HPR-120kN, and (e) average local misorientation angle for each rolling condition.

recrystallised grains and high-strain unrecrystallised zones leads to the formation of a banded KAM pattern, where strain localises in periodically distributed deformation-retained layers. At 120 kN, the deformation introduced far exceeds the strain-relief capacity of the thermal cycle. Although recrystallisation still occurs locally, producing equiaxed regions with low KAM values, large areas retain substantial deformation strain. As a result, the KAM distribution becomes even more strongly banded, consisting of alternating low-strain recrystallised bands and high-strain deformation-preserved layers. This indicates that at high rolling loads, recrystallisation becomes increasingly insufficient to eliminate the accumulated lattice distortion. Overall, the evolution of KAM with rolling load reflects a dynamic interplay between deformation accumulation and partial recrystallisation [32]. As the rolling load increases, recrystallised equiaxed regions consistently exhibit lower local strain [33,34], whereas unrecrystallised regions retain significant deformation misorientation, giving rise to the progressively more pronounced banded KAM distributions in the 80 kN and 120 kN conditions.

Besides, the distribution of the average local misorientation angles is displayed in Fig. 6(e). From that, the unrolled wall shows a narrow peak near 0°, whereas the rolled samples exhibit progressively broader and right-shifted curves toward higher misorientation angles with increasing rolling force. This continuous rightward shift indicates an increase in dislocation density and stored strain energy, consistent with EBSD-based KAM analyses of rolled or peened w-DED 316L [18]. Based on mean KAM values obtained from each condition and using the equation of:

$$\rho_{GND} = \frac{2^{*}KAM_{ave}}{\mu b} \quad (1)$$

Where μ is the step size (0.8 μm) applied in the EBSD mapping and b represents the Burger vector, which is 0.255 nm [35], the corresponding GND densities were estimated to be approximately 8.8×10^{13}, 1.2×10^{14}, 2.0×10^{14}, and 3.0×10^{14} m^{-2}, respectively. This represents roughly a threefold increase in dislocation density from the unrolled wall to the 120 kN condition, providing the microstructural basis for the subsequent enhancement in hardness and strength.

3.3. Mechanical properties in as-deposited condition

The hardness distributions under different interlayer rolling conditions are presented in Fig. 7. Each hardness map was obtained from three vertical measurement lines positioned at the wall centre and ±3 mm from the midline, with indentations performed every 0.5 mm along the build direction. In the hardness maps, the colour gradients represent the local Vickers hardness values across the cross-sections. In the wall deposited without rolling (Fig. 7(a)), the hardness remains relatively low, averaging 178.3 HV. Besides, a weakly banded pattern is observed along the build height, corresponding to the layer-by-layer deposition sequence and reflecting the thermal history of cyclic reheating. Further, a slight decrease in hardness toward the top is consistent with the cumulative thermal cycling experienced by the upper layers during deposition, where repeated reheating promotes local recovery and mild substructure coarsening. At this stage, the microstructure is mainly characterised by epitaxial solidification and the absence of significant plastic deformation, as indicated by the columnar γ-austenite and interdendritic δ-ferrite observed in Fig. 4(a) and the coarse elongated

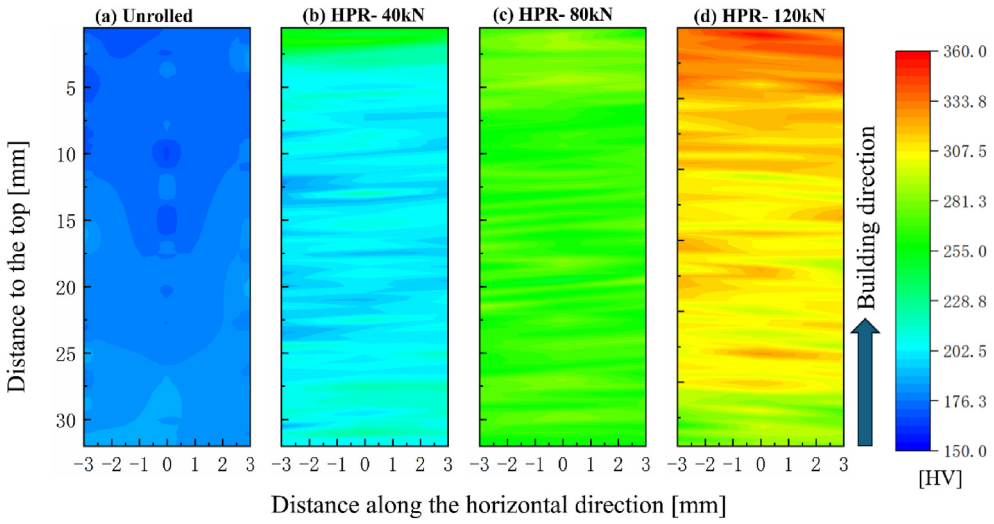

Fig. 7. Micro-hardness distribution of w-DED 316L walls deposited under different rolling forces: (a) Unrolled, (b) HPR-40 kN, (c) HPR-80 kN, and (d) HPR-120 kN.

grains revealed by EBSD in Fig. 5(a).

When a rolling force of 40 kN was applied (Fig. 7(b)), the average hardness increased to 206.7 HV, accompanied by the appearance of horizontally oriented streaks across the section. These streaks indicate localised strain bands introduced by interlayer compression. The enhancement arises from dislocation accumulation and substructural distortion within the γ-austenite matrix, consistent with the bent dendritic morphologies and fragmented grains observed in Fig. 4(c and d) and 5(b). In addition, the periodic hardness banding became less distinct, which indicates a gradual shift in the dominant mechanism from thermal history to deformation-induced hardening. At 80 kN (Fig. 7(c)), the hardness further rises to 268.2 HV, and the overall distribution becomes more homogeneous. The green-dominated colour zone indicates uniform deformation transmission through successive layers. Such hardness homogenisation reflects the formation of refined subgrain structures with reduced aspect ratios, whereas the elevated GND density (Fig. 6) demonstrates that the strengthening mechanism is dominated by dislocation strain hardening [36,37]. Under the maximum applied rolling force of 120 kN (Fig. 7(d)), the wall exhibits an average hardness of 309.8 HV, representing an increase of approximately 74% compared with the unrolled condition. The hardness field appears continuous along both horizontal and vertical directions, indicating that the imposed strain was effectively distributed throughout the build height.

In contrast to the unrolled condition, the rolled walls display slightly higher hardness in the upper regions than in the lower ones. This hardness gradient is attributed to the temperature-dependent deformation behaviour during in-process rolling. The upper layers, which remain at elevated temperature immediately after deposition, accommodate larger effective plastic strain under the same applied load, leading to a higher dislocation density and consequently greater hardness near the surface. In comparison, the lower regions, being cooler and mechanically stiffer, undergo less deformation, which results in a gradual decrease in hardness towards the bottom [38]. Overall, the hardness evolution demonstrates that HPR significantly improves both the strength and uniformity of the w-DED 316L walls. The gradual increase in hardness and its spatial homogenisation are consistent with the EBSD evidence of grain subdivision and the dislocation density. These findings illustrate that mechanical deformation becomes the primary driver of microstructural evolution once rolling is applied, establishing a clear link between microstructural distortion and macroscopic strengthening to be further examined in the subsequent tensile analysis.

Fig. 8 illustrates the tensile behaviour of the w-DED 316L walls under various rolling conditions. With increasing rolling force, the yield strength (YS) and ultimate tensile strength (UTS) increase continuously from approximately 300 MPa and 500 MPa in the unrolled condition to about 670 MPa and nearly 900 MPa at the highest rolling force, respectively, while the elongation to fracture decreases from ~56% to ~20%, indicating a strength-ductility trade-off. This strengthening development results from rolling-induced strain hardening associated with interlayer compression, which introduces a high density of dislocations and promotes the formation of subgrains. The strengthening

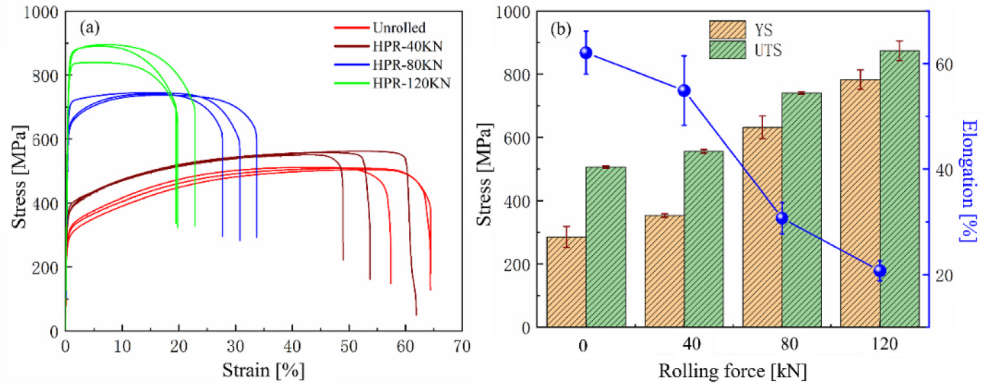

Fig. 8. (a) Strain-stress curves of w-DED 316L stainless steel walls deposited under different rolling forces; (b) Summary of tensile results under different rolling conditions.

trend is consistent with the hardness enhancement observed in Fig. 7(b) as well. With increasing rolling severity, more effective plastic deformation further elevates the stored strain energy and leads to significant compression and segmentation of the δ-ferrite network, contributing to additional strengthening. At higher rolling forces, the mechanical response becomes increasingly dominated by accumulated strain energy and restricted dislocation recovery during deposition, resulting in a marked reduction in ductility [39]. The high strength levels achieved without the appearance of fracture indicate that the imposed rolling does not introduce detrimental defects such as cracking. To further customise the performance of the deposited material toward practical application requirements, a post-heat treatment was therefore introduced. The subsequent section examines the synergistic effects of in-process rolling and heat treatment on microstructure evolution and mechanical properties.

3.4. Microstructural comparison in as-deposited and heat-treated conditions

Fig. 9 compares the microstructures of the unrolled and 120 kN rolled samples before and after heat treatment, showing the synergistic effect between in-process rolling and post heat treatment on microstructural control. In the unrolled as-deposited condition (Fig. 9(a)), the microstructure is characterised by the elongated γ-austenite columnar and continuous δ-ferrite dendritic structure. After applying 120 kN rolling (Fig. 9(b)), the solidification morphology was significantly compressed, indicating strong plastic deformation. After heat treatment, the unrolled sample (Fig. 9(c)) presents partial coarsening and spheroidisation of δ-ferrite with unchanged coarse columnar γ-austenite. In contrast, the rolled and heat-treated sample (Fig. 9(d)) exhibits a fully recrystallised γ-austenite microstructure with equiaxed grains and refined δ-ferrite particles. All dendritic structures disappeared, indicating that recrystallisation is strongly activated when sufficient deformation has been introduced beforehand. Overall, the direct comparison between unrolled and 120 kN rolled conditions shows that rolling provides the necessary deformation energy for subsequent recrystallisation, transforming the solidification-dominated structure into a uniform, equiaxed microstructure after heat treatment.

The austenite IPF maps and quantitative grain morphology statistics of the samples after heat treatment under different rolling conditions are compared in Fig. 10. In the unrolled heat-treated condition (Fig. 10(a)), the microstructure remains dominated by coarse columnar austenite grains with the average ECD over 2.3 mm (Fig. 10(e)), even after heat treatment. Only limited boundary recovery is observed, indicating that the residual thermal strain energy from layer-by-layer deposition is insufficient to drive recrystallisation. With in-process rolling (Fig. 10 (b–d)), the deformation fundamentally alters the microstructure evolution during heat treatment. At 40 kN, the columnar grains are partially fragmented and locally replaced by small equiaxed regions, with the average grain size reduced to 158 μm (Fig. 10(e)). Correspondingly, the AR value (Fig. 10(f)) decreases notably compared with the unrolled sample, reflecting the onset of recrystallisation and partial elimination of the solidification-induced anisotropy. At 80 kN and 120 kN, the microstructure becomes fully equiaxed and homogeneous, indicating complete recrystallisation. The average grain size decreases significantly to 27 μm and 24 μm, respectively, while the AR distributions converge around unity, confirming the formation of an isotropic grain morphology. The columnar texture inherited from solidification is replaced by a fine, randomly oriented austenitic grain structure, confirming that mechanical deformation dominates the subsequent thermal response. Increasing the rolling force generates high dislocation densities, subgrain boundaries, and lattice curvature, all of which serve as effective nucleation sites for static recrystallisation during heat treatment.

Upon further magnification, a systematic evolution of the grain boundary distribution with increasing rolling load after heat treatment can be observed (Fig. 11). After heat treatment, the unrolled sample (Fig. 11(a–e)) largely retains elongated grains with relatively sparse high-angle and Σ3 coincidence site lattice (CSL) boundaries, indicating that the stored energy in the as-deposited columnar structure is insufficient to drive extensive recrystallisation. By contrast, the rolled samples (40-120 kN, Fig. 11(b–d, f-h)) show progressively more refined and equiaxed microstructures after heat treatment, together with a much denser and more homogeneous grain boundary network.

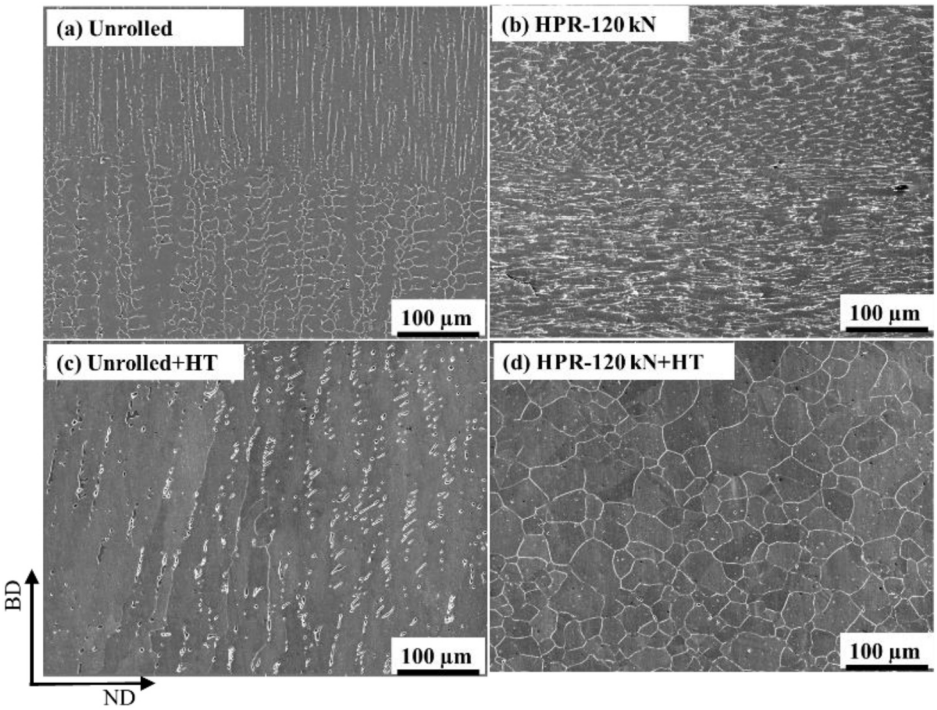

Fig. 9. SEM observations under different conditions: (a) Unrolled, (b) HPR-120kN, (c)Unrolled + HT, and (d) HPR-120kN + HT.

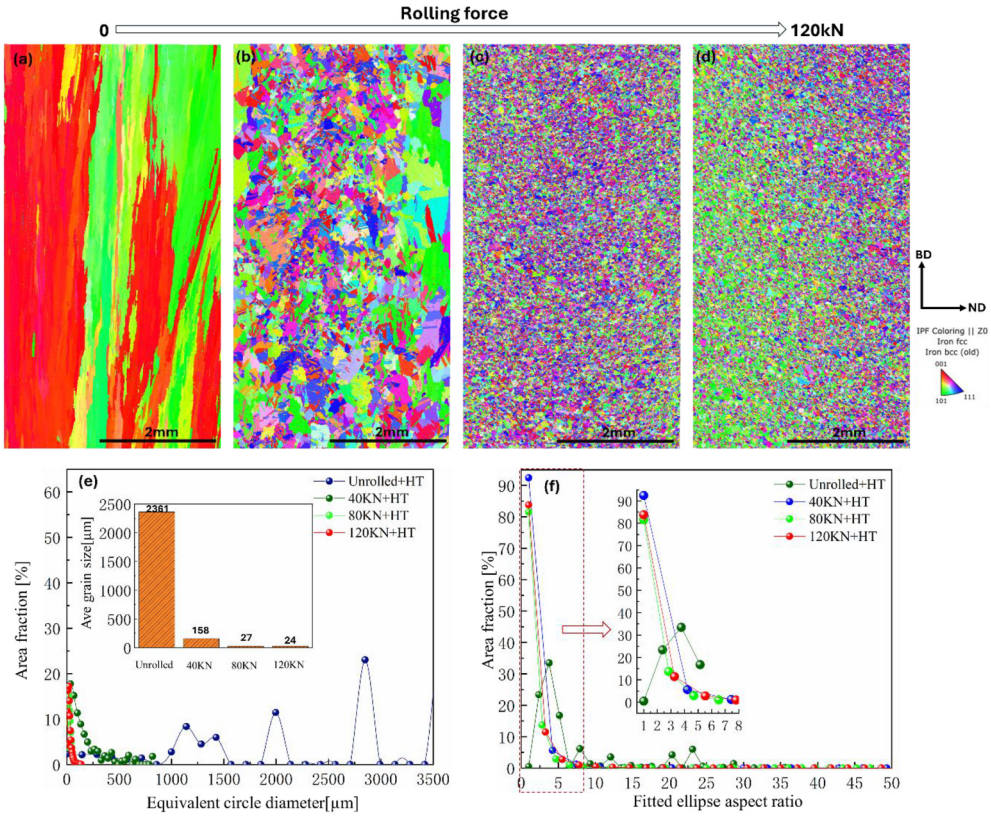

Fig. 10. IPF maps after heat treatment under various rolling conditions: (a) Unrolled, (b) HPR-40kN, (c) HPR-80kN, and (d) HPR-120kN; (e) comparison of ECD distributions in different conditions; (f) comparison of fitted ellipse AR distributions in different conditions.

This transformation is directly related to the level of strain energy introduced by rolling. As shown in the as-deposited misorientation distributions (Fig. 11(i)) and the low/high angle grain boundaries (LAGB/HAGB) fractions (Fig. 11(k)), rolling increases the fraction of LAGBs substantially, which correspond to subgrain boundaries formed through deformation and dislocation rearrangement [40]. These boundaries act as nuclei for recrystallisation during the subsequent heat treatment. The misorientation distributions (Fig. 11(j)) and the boundary fractions in Fig. 11(l) show that 80-120 kN rolling significantly accelerates the conversion of LAGBs into HAGBs and Σ3 CSL boundaries. The substantial increase in Σ3 boundaries observed at high rolling loads after heat treatment arises from the strong coupling between deformation-induced stored energy and annealing twinning mechanisms in FCC alloys with low stacking-fault-energy (SFE) [40–42]. Interlayer rolling at high loads introduces intense plastic deformation, leading to a high density of dislocations and the formation of numerous subgrain boundaries. These deformation structures significantly elevate the stored energy in the material, thereby providing a strong thermodynamic driving force for recrystallisation [43]. During annealing, these deformation-generated subgrain boundaries act as preferential nucleation sites for recrystallised grains [44]. Because 316L possesses relatively low SFE, the migration of recrystallising grain boundaries is prone to generating coherent Σ3 twin boundaries through repeated formation of stacking faults on {111} planes [45]. As rolling load increases, both the number of subgrain boundaries and the level of stored energy increase, enabling more extensive recrystallisation and, critically, more prolific annealing twinning. In summary, high rolling loads enrich the microstructure with deformation-induced substructures that supply both the driving force and favourable nucleation pathways for recrystallisation, while the heat treatment environment activates annealing twinning. The synergy between these two processes results in a dramatic increase in Σ3 boundaries, producing a twin-rich, high-HAGB microstructure that enhances isotropy and microstructural stability in w-DED 316L.

The crystallographic texture evolution before and after heat treatment under different rolling forces is shown in Fig. 12. In the as-deposited condition, the unrolled sample exhibits a strong <001> fiber texture parallel to BD, characteristic of epitaxial growth during directional solidification of austenitic stainless steel. This strong cube-like alignment ({001}<100>) results from the thermal gradient and epitaxial grain competition typical of w-DED processing. With increasing rolling force, this solidification texture progressively weakens and transitions toward classical rolling textures typical of FCC metals. At 40 kN, the appearance of scattered {112}<111> and {123}<634> orientations indicates the development of Copper-type (112)<111> and S-type (123)<634> components, associated with plane-strain deformation and dislocation slip. At 80 kN, these features become stronger, and additional traces of Brass-type (011)<211> and Goss-type (011)<100> orientations appear, reflecting more severe plastic deformation and lattice rotation toward the β-fiber ({112}–{011}) texture sequence. At 120 kN, the β-fiber is fully established, with deformation texture components distributed broadly between Copper and Brass orientations, consistent with extensive lattice curvature and high dislocation density observed in KAM maps.

After heat treatment, distinct texture relaxation and recrystallisation behaviour are observed. The unrolled sample retains the strong {001}<100> solidification texture, indicating minimal recrystallisation. In contrast, the rolled samples show significant weakening of the β-fiber and the emergence of annealing textures typical of FCC recrystallisation. At 80 kN and 120 kN, newly formed equiaxed grains exhibit weak Cube (001)<100>, Rotated Cube (001)<110>, and scattered Goss (011)<100> components, reflecting strain-induced recrystallisation and subgrain growth. The overall orientation distribution becomes nearly random, indicating that recrystallisation consumes the deformation-stored energy and erases prior rolling textures.

These results demonstrate that in-process rolling transforms the

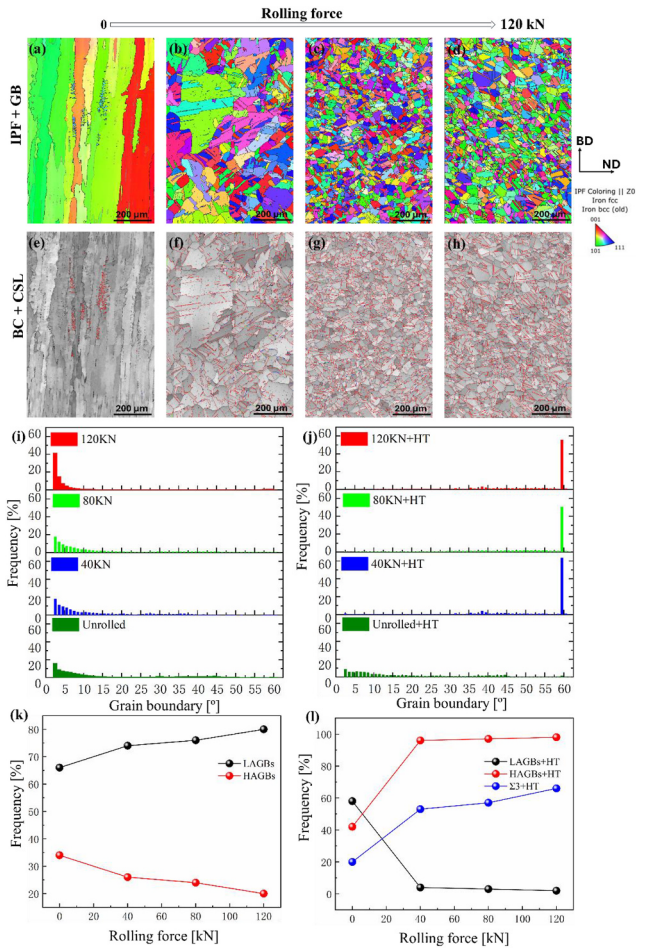

Fig. 11. High-magnification EBSD IPF + GB (grain boundary) and BC + CSL (band contrast + coincidence site lattice) maps of heat-treated 316L walls deposited under different interlayer rolling conditions: (a, e) no rolling, (b, f) 40 kN, (c, g) 80 kN, (d, h) 120 kN; comparison of misorientation angle distributions of (i) as-deposited and (j) heat-treated 316L walls under different interlayer rolling conditions; quantitative fractions of LAGBs, HAGBs and Σ3 boundaries as a function of rolling force in (k) as-deposited and (l) heat-treated conditions.

original epitaxial <001> solidification texture into a deformation-induced β-fiber (Copper–S–Brass) rolling texture, which upon subsequent heat treatment evolves into Cube- and Goss-type recrystallisation textures. This sequential transition from epitaxial → rolling → annealing textures confirms the strong thermo-mechanical coupling in w-DED 316L stainless steel and explains the improved isotropy and ductility achieved in rolled + heat-treated samples.

3.5. *Comparison of mechanical properties in as-deposited, heat-treated and previous work*

Fig. 13(a and b) summarise the room-temperature tensile response of all processing conditions and establishes a direct link between the microstructural evolution presented in Figs. 4–10 and the resultant macroscopic properties. The increase in YS and UTS with rolling force in the as-deposited condition is closely associated with the microstructural refinement induced by interlayer rolling. Compared with the unrolled wall, the substantial reduction in grain size, increase in GND density and breakdown of the coarse columnar structure collectively enhance the resistance to plastic deformation, thereby increasing the load-bearing capacity of the deposited walls. The strengthening effect becomes particularly pronounced at rolling forces of 80 and 120 kN, where both grain refinement strengthening and dislocation strengthening contribute significantly to the observed increase in strength.

For most conditions, the stress-strain curves shift toward lower strength and markedly higher elongation. At 120 kN, heat treatment reduces UTS from ~900 MPa to ~600 MPa, while elongation increases from 20.7% to 72.6%, representing a threefold increase in ductility. A key factor behind this remarkable ductility restoration and the simultaneous enhancement in strength and elongation relative to the unrolled condition is the formation of abundant Σ3 CSL boundaries after heat treatment [46]. As low-energy and highly coherent interfaces, Σ3 boundaries act as effective barriers to dislocation motion while preserving excellent crystallographic compatibility across neighbouring grains [47]. This unique combination enables strengthening without sacrificing ductility, unlike randomly oriented HAGBs. Furthermore, the high density of Σ3 boundaries promotes more homogeneous deformation by facilitating coordinated activation of multiple {111}<110> slip systems, thereby improving strain compatibility and delaying localised necking. Their presence also contributes to thermally stable interfaces that resist crack nucleation. The synergy between deformation-induced stored energy and annealing-driven twin formation is thus central to the superior tensile performance achieved at high rolling forces.

After heat treatment, the tensile responses of the rolled samples show recovery in ductility accompanied by a reduction in strength. While the unrolled material presents only tiny changes in both strength and elongation after heat treatment, the rolled conditions display a substantial increase in elongation, from approximately 56% in the as-built state to about 72% after heat treatment. This behaviour indicates that the mechanical response after heat treatment is primarily governed by the release and redistribution of stored energy introduced by interlayer rolling. In the rolled samples, heat treatment promotes dislocation recovery, substructural reorganisation, and the formation of more favourable grain boundary configurations, thereby restoring ductility while reducing the strengthening contribution from deformation-induced defects. As a result, the strength levels of the rolled samples converge after heat treatment, whereas their elongation is significantly enhanced. In addition, the TRIP effect may also contribute to the favourable strength-ductility combination observed in the present study. Previous studies have shown that deformation-induced martensitic transformation in austenitic stainless steels can enhance strain hardening and delay localised deformation, thereby improving toughness and ductility [48]. Notably, the 40 kN condition exhibits a slightly different trend, where the heat-treated sample shows a higher UTS despite a lower YS compared with the corresponding as-deposited state. In the as-deposited 40 kN sample, interlayer rolling introduced deformation strengthening through increased dislocation density, resulting in a relatively high YS. After heat treatment, recovery and substructural reorganisation reduced the strengthening contribution from deformation-induced dislocations, leading to a lower YS. At the same time, the heat treatment improved deformation compatibility and strain-hardening behaviour during tensile deformation, which delayed localised deformation and resulted in a slightly higher UTS compared with the corresponding as-deposited condition. In contrast, the 80 and 120 kN samples already exhibited substantial deformation strengthening in the as-deposited state. After heat treatment, the reduction in deformation-induced strengthening became more dominant, leading to decreases in both YS and UTS, although the ductility was significantly improved. In contrast, the unrolled material, which contains a relatively low level of deformation-induced defects in the as-built condition. This illustrates limited sensitivity to heat treatment, leading to only minor changes in mechanical properties.

The comparison with the literature in Fig. 13(c and d) highlights the distinctiveness of this hybrid strategy. The previous studies include laser metal deposition shaping (LMDS) [49], selective laser melting (SLM) processing [50], laser melting and laser cladding (LMLC) deposition [51], DED process [52], LENS deposition process [53], synchronous-hammer-forging-assisted LDED (SH-LDED) [54], laser

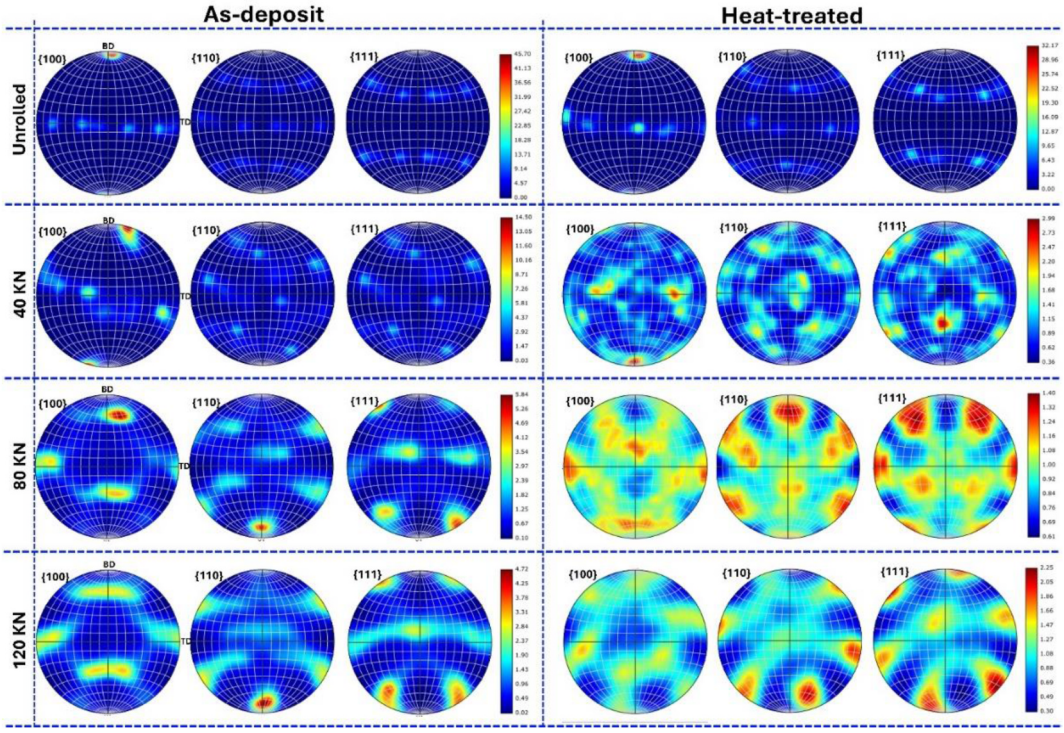

Fig. 12. Evolution of crystallographic texture under different rolling forces before and after heat treatment.

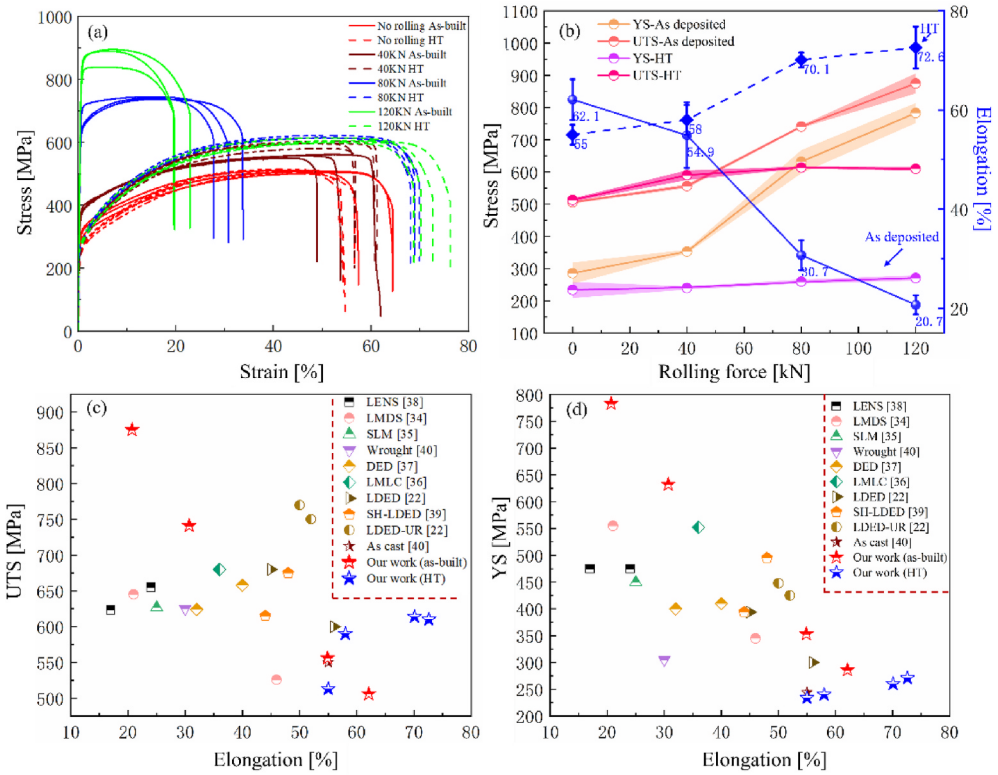

Fig. 13. (a) and (b) tensile properties of w-DED 316L before and after heat treatment under different rolling forces; (c) and (d) comparison with previous studies.

directed energy deposition-ultrasonic rolling (LDED-UR) [22], as cast and wrought [55]. The as-rolled walls position in the high-strength region of reported AM 316L, while the heat-treated counterparts display ductility values (60-72%) that are approximately twice those of typical AM 316L steels at similar strength levels, and even surpass wrought 316L in elongation while maintaining competitive strength. This broad property envelope ranging from ultra-high strength in the as-rolled condition to balanced strength-ductility after heat treatment validates that HPR combined with a suitable thermal schedule enables application-oriented customisation within a single w-DED workflow.

Thus, Fig. 13 indicates that the hybrid HPR + HT approach provides a robust, controllable pathway for tailoring microstructure and mechanical performance in w-DED 316L. The method enables property combinations that are difficult to achieve through conventional additive processes and offers a versatile platform for the design of high-performance AM stainless-steel components.

The present results demonstrate that HPR, combined with a subsequent solution heat treatment, provides an efficient and highly controllable thermo-mechanical route to tailor the process-microstructure-property relationship of w-DED 316L stainless steel. Unlike conventional WAAM builds dominated by solidification and thermal cycling, the introduction of cold rolling fundamentally alters the balance between solidification, deformation and recovery, thereby enabling microstructural engineering over a wide range of strength and ductility levels. Compared with previously reported hot inter-pass rolling approaches, the present cold high-pressure rolling strategy offers both mechanistic and practical advantages [18]. Rolling at a low, controlled temperature avoids exposing the roller to severe thermal loads, simplifies temperature control, and eliminates the need for complex heating arrangements. More importantly, from a microstructural standpoint, deformation, recrystallisation and final grain size can be decoupled and independently tuned by adjusting rolling force and heat-treatment parameters. This separation of deformation and thermal activation provides a more flexible and predictable route for property customisation. Overall, by combining HPR with post-deposition solution heat treatment, this work establishes a clear and controllable pathway to transform the coarse, anisotropic solidification microstructure of w-DED 316L into a fine, nearly isotropic recrystallised austenitic structure. The as-deposited rolled walls exploit a combination of grain refinement strengthening, dislocation strengthening and subgrain strengthening to achieve high strength, while the rolled and heat-treated walls realise a superior strength-ductility balance that matches or exceeds wrought 316L and clearly surpasses conventional WAAM 316L. This positions cold in-process rolling coupled with heat treatment as a practical and industry-relevant thermo-mechanical strategy for high-performance 316L components produced by w-DED.

4. Conclusions

This study demonstrates that HPR, combined with a simple post-deposition heat treatment, provides an effective and industrially practical strategy for microstructure and property control in w-DED 316L stainless steel. The approach integrates mechanical deformation with thermal activation to overcome the inherent limitations of DED solidification microstructures and enables application-oriented performance tailoring within a single manufacturing route. The outcomes can be summarised as follows:

1. The investigated HPR strategy enables a broad and continuous mechanical property window, allowing effective customisation of strength and ductility in w-DED 316L. The combined HPR + HT route achieves a superior strength-ductility balance that surpasses most reported AM 316L and rivals wrought material. From an industrial perspective, the hybrid HPR + HT route is compatible with large-scale wire-DED systems, does not require complex thermal cycles, and enables on-demand tailoring of mechanical performance.
2. Cold HPR provides a fundamentally different and more effective thermo-mechanical pathway than hot inter-pass rolling. By introducing a large plastic strain interlayer, cold HPR suppresses dynamic recovery during deposition, enables substantial accumulation of stored strain energy, and allows recrystallisation to be deliberately activated during subsequent heat treatment, thereby offering superior control over microstructural evolution and process robustness.
3. In the as-deposited condition, HPR fundamentally restructures the solidification-derived microstructure through deformation-driven grain subdivision rather than recrystallisation. Interlayer boundaries are straightened, γ-austenite grains are compressed and fragmented, and δ-ferrite networks are disrupted, reducing the effective grain size at 120 kN and markedly increasing the fractions of low-angle grain boundaries and geometrically necessary dislocations.
4. Post-heat treatment promotes extensive recrystallisation in the rolled samples, reflecting the critical role of rolling-induced stored strain energy, while the unrolled wall undergoes grain coarsening without evidence of extensive recrystallisation. The heavily rolled samples develop fine equiaxed γ-austenite grains with high fractions of high-angle and Σ3 boundaries, indicating that cold HPR establishes the necessary microstructural preconditions for strain-induced recrystallisation.

CRediT authorship contribution statement

Yao Lu: Conceptualization, Data curation, Formal analysis, Investigation, Methodology, Validation, Visualization, Writing – original draft. **Jun Wang:** Conceptualization, Data curation, Formal analysis, Investigation, Methodology, Supervision, Validation, Writing – review & editing. **Hanxing Zhang:** Data curation, Investigation. **Jialuo Ding:** Conceptualization, Methodology, Resources. **Stewart Williams:** Conceptualization, Funding acquisition, Methodology, Project administration, Resources, Supervision, Writing – review & editing.

Declaration of competing interest

The authors declared that they have no conflicts of interest and have no commercial or associative interest that represents a conflict of interest in connection with the work submitted.

Acknowledgement

The authors would like to thank the technical support from Mark Allen, Kris Bramley and Steve Pope.

Data availability

Data will be made available on request.

References

[1] W.E. Frazier, Metal additive manufacturing: a review, J. Mater. Eng. Perform. 23 (6) (2014) 1917–1928.
[2] T. DebRoy, et al., Additive manufacturing of metallic components – process, structure and properties, Prog. Mater. Sci. 92 (2018) 112–224.
[3] T. Özel, et al., A review on wire-fed directed energy deposition based metal additive manufacturing 7 (1) (2023) 45.
[4] J. Wang, et al., Insights into crack prevention and property improvement for additively manufactured ultra-high-strength steel structures with complex geometries, Additive Manufacturing Letters 14 (2025) 100307.
[5] J. Wang, et al., On the composition gradient of steel/Invar functionally graded material manufactured by wire-based direct energy deposition, Addit. Manuf. 96 (2024) 104594.
[6] Y. Lu, et al., Additive manufacturing of a functionally graded high entropy alloy using a hybrid powder-bed wire-based direct energy deposition approach, Addit. Manuf. 63 (2023) 103424.
[7] A. Saboori, et al., Microstructure and Mechanical Properties of AISI 316L Produced by Directed Energy Deposition-based Additive Manufacturing: a Review, 2020, 10 (9): p. 3310.
[8] D.J.M. D'Andrea, Additive manufacturing of AISI 316L stainless steel: a review 13 (8) (2023) 1370.
[9] M. Naghizadeh, H. Mirzadeh, Microstructural evolutions during reversion annealing of cold-rolled AISI 316 austenitic stainless steel, Metall. Mater. Trans. 49 (6) (2018) 2248–2256.
[10] S.W. Williams, et al., Wire + Arc Additive Manufacturing, Mater. Sci. Technol. 32 (7) (2016) 641–647.
[11] V.R. Duarte, et al., Hot forging wire and arc additive manufacturing (HF-WAAM), Addit. Manuf. 35 (2020) 101193.
[12] J.P. Oliveira, T.G. Santos, R.M. Miranda, Revisiting fundamental welding concepts to improve additive manufacturing: from theory to practice, Prog. Mater. Sci. 107 (2020) 100590.

[13] B.P. Nagasai, S. Malarvizhi, V. Balasubramanian, Effect of welding processes on mechanical and metallurgical characteristics of carbon steel cylindrical components made by wire arc additive manufacturing (WAAM) technique, CIRP J. Manuf. Sci. Technol. 36 (2022) 100–116.
[14] L. Wang, J. Xue, Q. Wang, Correlation between arc mode, microstructure, and mechanical properties during wire arc additive manufacturing of 316L stainless steel, Mater. Sci. Eng., A 751 (2019) 183–190.
[15] X. Chen, et al., Microstructure and mechanical properties of the austenitic stainless steel 316L fabricated by gas metal arc additive manufacturing, Mater. Sci. Eng., A 703 (2017) 567–577.
[16] C. Wang, et al., Study on microstructure and tensile properties of 316L stainless steel fabricated by CMT wire and arc additive manufacturing, Mater. Sci. Eng., A 796 (2020) 140006.
[17] B.D. Bankong, et al., Review of post-processing methods for high-quality wire arc additive manufacturing 39 (2) (2023) 129–146.
[18] H. Xu, et al., Effect of in-situ rolling and heat treatment on microstructure, mechanical and corrosion properties of wire-arc additively manufactured 316L stainless steel, J. Mater. Res. Technol. 27 (2023) 3349–3361.
[19] F.W.C. Farias, T.J.G. dos Santos, J.P. Oliveira, Directed energy deposition + mechanical interlayer deformation additive manufacturing: a state-of-the-art literature review, Int. J. Adv. Manuf. Technol. 131 (3) (2024) 999–1038.
[20] J. Wang, et al., Acquisition of HSLA steel weld joints with excellent mechanical performance through flash butt welding physical simulation, Mater. Lett. 303 (2021) 130511.
[21] W.H. Kan, et al., Effect of in-situ layer-by-layer rolling on the microstructure, mechanical properties, and corrosion resistance of a directed energy deposited 316L stainless steel, Addit. Manuf. 55 (2022) 102863.
[22] G. Liu, et al., Achieving high strength 316L stainless steel by laser directed energy deposition-ultrasonic rolling hybrid process, Mater. Sci. Eng., A 903 (2024) 146665.
[23] S. Pradhan, D. Dhupal, Machining of aluminium nitride ceramic with a hAJM process using SiC abrasives: experiments and simulation, J. Manuf. Process. 95 (2023) 68–90.
[24] N. Bastola, et al., A review of the residual stress generation in metal additive manufacturing: analysis of cause, measurement, effects, and prevention, Micromachines 14 (2023) 1480, https://doi.org/10.3390/mi14071480.
[25] L. Nguyen, et al., Analysis and compensation of shrinkage and distortion in wire-arc additive manufacturing of thin-walled curved hollow sections, Addit. Manuf. 47 (2021) 102365.
[26] L. Li, et al., Progress in cold roll bonding of metals 9 (2) (2008) 023001.
[27] L. Zixuan, et al., Recent advances and trends in roll bonding process and bonding model: A review 36 (4) (2023) 36–74.
[28] X. Chen, et al., Effect of heat treatment on microstructure, mechanical and corrosion properties of austenitic stainless steel 316L using arc additive manufacturing, Mater. Sci. Eng., A 715 (2018) 307–314.
[29] Y. Guo, et al., Formability, microstructure evolution and mechanical properties of wire arc additively manufactured AZ80M magnesium alloy using gas tungsten arc welding, J. Magnesium Alloys 9 (1) (2021) 192–201.
[30] Y. Lu, et al., Simulation, microstructure and austenite reconstruction of a medium carbon micro-alloyed steel subjected to an austenitising bending process, Mater. Lett. 305 (2021) 130772.
[31] S.C. Schwarm, et al., Characterization of Phase Properties and Deformation in ferritic-austenitic Duplex Stainless Steels by Nanoindentation and Finite Element Method, vol. 680, 2017, pp. 359–367.
[32] Z. Wang, et al., Grain boundary-induced stress localization during compression deformation of polycrystalline 316L stainless steel, Appl. Phys. A 130 (12) (2024) 870.
[33] L. Cui, et al., Revealing relationships between microstructure and hardening nature of additively manufactured 316L stainless steel, Mater. Des. 198 (2021) 109385.
[34] M.A. Steiner, et al., Monte Carlo modeling of recrystallization processes in α-uranium, J. Nucl. Mater. 492 (2017) 74–87.
[35] H. Yi, et al., Good strength-ductility synergy achieved in a Fe62Ni16Co9Mn9Ti3Si1 Fe-high-entropy alloy with heterogeneous structures, J. Mater. Res. Technol. 30 (2024) 8488–8499.
[36] Y. Lu, et al., Influence of hot compressive parameters on flow behaviour and microstructure evolution in a commercial medium carbon micro-alloyed spring steel, J. Manuf. Process. 58 (2020) 1171–1181.
[37] K.M. Bertsch, et al., Origin of dislocation structures in an additively manufactured austenitic stainless steel 316L, Acta Mater. 199 (2020) 19–33.
[38] A. Delissen, et al., Realization and assessment of metal additive manufacturing and topology optimization for high-precision motion systems, Addit. Manuf. 58 (2022) 103012.
[39] H. Wu, G. Fan, An overview of tailoring strain delocalization for strength-ductility synergy, Prog. Mater. Sci. 113 (2020) 100675.
[40] Y. Yang, et al., Revealing the microstructure evolution mechanism and mechanical responses of a novel Al–Zn–Mg–Cu alloy by hot deformation process, J. Mater. Res. Technol. 29 (2024) 3699–3710.
[41] N.K. Sharma, S. Shekhar, New insights into the evolution of twin boundaries during recrystallization and grain growth of low-SFE FCC alloys, Mater. Charact. 159 (2020) 110015.
[42] H. Xie, et al., A New Criterion for Formation Capability of Annealing Twin in face-centered Cubic metals/alloys, 278, 2024 120245.
[43] R. Doherty, et al., Current issues in recrystallization: a review 238 (2) (1997) 219–274.
[44] F.J. Humphreys, M. Hatherly, Recrystallization and Related Annealing Phenomena, elsevier, 2012.
[45] K.H. Lo, C.H. Shek, J.K.L. Lai, Recent developments in stainless steels, Mater. Sci. Eng. R Rep. 65 (4) (2009) 39–104.
[46] T.J.J.o.m.s. Watanabe, Grain boundary engineering: historical perspective and future prospects 46 (12) (2011) 4095–4115.
[47] V.J.M.s. Randle, And technology, Role of grain boundary plane in grain boundary engineering 26 (7) (2010) 774–780.
[48] M. Naghizadeh, H. Mirzadeh, Effects of grain size on mechanical properties and work-hardening behavior of AISI 304 austenitic stainless steel 90 (10) (2019) 1900153.
[49] K. Zhang, et al., Characterization of stainless steel parts by Laser Metal Deposition Shaping, Mater. Des. 55 (2014) 104–119.
[50] R. Casati, J. Lemke, M. Vedani, Microstructure and fracture behavior of 316L austenitic stainless steel produced by selective laser melting, J. Mater. Sci. Technol. 32 (8) (2016) 738–744.
[51] M. Ma, Z. Wang, X. Zeng, A comparison on metallurgical behaviors of 316L stainless steel by selective laser melting and laser cladding deposition, Mater. Sci. Eng., A 685 (2017) 265–273.
[52] A. Saboori, et al., An investigation on the effect of deposition pattern on the microstructure, mechanical properties and residual stress of 316L produced by Directed Energy Deposition, Mater. Sci. Eng., A 780 (2020) 139179.
[53] N. Yang, et al., Process-Structure-Property relationships for 316L stainless steel fabricated by additive manufacturing and its implication for component engineering, J. Therm. Spray Technol. 26 (4) (2017) 610–626.
[54] D. Wu, et al., Synchronous-hammer-forging-assisted laser directed energy deposition additive manufacturing of high-performance 316L samples, J. Mater. Process. Technol. 307 (2022) 117695.
[55] D. Benjamin, Metals Handbook: Properties and Selection: Stainless Steels, Tool Materials and special-purpose Metals, American Society for Metals, 1980.

DSPACE

https://dspace.org/

Achieving superior performance of wire-directed energy deposited 316L stainless steel through the synergic effect of in-process high-pressure rolling and post-heat treatment

Lu, Yao; Wang, Jun; Zhang, Hanxing; Ding, Jialuo; Williams, Stewart W.

2026-09
Elsevier
https://doi.org/10.1016/j.msea.2026.150575
Lu Y, Wang J, Zhang H, et al., (2026) Achieving superior performance of wire-directed energy deposited 316L stainless steel through the synergic effect of in-process high-pressure rolling and post-heat treatment. Materials Science and Engineering: A, Volume 971, September 2026, Article number 150575

Downloaded from a DSpace repository. https://dspace.org/